



CrossMark  
click for updates

Cite this: *Anal. Methods*, 2015, 7, 9304

# Structural differences in archaeologically relevant calcite†

Ben Xu,<sup>a</sup> Michael B. Toffolo,<sup>‡b</sup> Lior Regev,<sup>b</sup> Elisabetta Boaretto<sup>\*b</sup>  
and Kristin M. Poduska<sup>\*a</sup>

We show that two different sources of calcite (geogenic flowstones and anthropogenic lime plaster) have complex, yet distinctive, structural disorder signatures. It is effective to identify these differences by pairing a rapid, fieldwork-compatible technique (Fourier transform infrared (FTIR) spectroscopy) with a robust laboratory-based technique (X-ray diffraction (XRD) peak width analyses). We demonstrate that crystalline domain size, microstrain fluctuations, and lattice strain each affect the FTIR spectra of calcite. To focus on each variable separately, XRD data and FTIR absorption spectra are compared among calcite samples formed by different processes. Small crystalline domain sizes cause changes to FTIR peak intensity ratios (grinding curves). However, larger microstrain fluctuations or larger lattice strain also produce similar changes. Thus, inferring structural differences from calcite FTIR spectra alone is not advisable. Instead, we advocate using FTIR grinding curves in conjunction with analyses of angle-dependent XRD peak widths using the Williamson–Hall relation. Thus, combining these two analysis techniques is more powerful and informative than using either one alone. These findings are relevant for heritage science, including archaeology.

Received 24th July 2015  
Accepted 30th September 2015

DOI: 10.1039/c5ay01942g

www.rsc.org/methods

## 1 Introduction

The origin of a material is of critical importance for archaeological interpretations, yet it is often challenging to determine. Calcite is especially difficult because it has many possible sources, including lime plaster (mortar), ash from fires,<sup>1</sup> speleothems (flowstones, stalactites, stalagmites), pedogenic sources (calcrete), and mineralized tissue (shells, otoliths).<sup>2</sup> This means that one must rely on subtle aspects of a material's structure, such as isotopic signatures,<sup>3</sup> trace elements, or heat-related changes to crystalline structure,<sup>4</sup> to determine possible formation pathways. An increasing number of studies investigate how structural order differences might be extracted from the vibrational signatures of solids through their Fourier transform infrared (FTIR) spectra.<sup>4–10</sup> In archaeological samples, there is strong empirical evidence that FTIR analyses are useful for distinguishing between lime plaster, ash, limestone, and sparry calcite.<sup>4,8</sup> However, the exact structural

differences that cause changes in the FTIR spectra have not yet been reported.

FTIR spectroscopy is an effective, non-destructive technique to characterize the composition of solid samples.<sup>11–14</sup> It offers the advantages of small sample size and portability, including on-site use during archaeological excavations and in art galleries.<sup>2,3,15,16</sup> However, quantitative analyses from FTIR data must be done carefully because peak intensities are strongly affected by sample preparation and measurement methods.<sup>4,8,17</sup> In this study, we show that three separate factors can contribute to FTIR peak intensities for calcite (CaCO<sub>3</sub>) samples. From these comparisons, we offer recommendations for future analyses to use FTIR in tandem with X-ray diffraction (XRD) data. Our recommendations are particularly relevant for archaeological investigations in calcite-rich environments such as caves.

Several studies have used density functional theory (DFT) in conjunction with group theory analyses to verify the energies and intensities of the IR-active vibrational modes expected for carbonate units in calcite.<sup>18,19</sup> Other studies have paired DFT calculations with experimental studies to investigate not only the mean vibrational energy for each mode (peak position), but also how IR peak widths can change when the calcite unit cell is distorted.<sup>7,8</sup> These studies show that calcite's in-plane carbonate bend ( $\nu_4$  mode) is strongly affected by deformation, which is consistent with experimental investigations of amorphous calcium carbonate from biogenic sources.<sup>7,20</sup> More recently, experimental studies of calcite showed that the same  $\nu_4$  peak is

<sup>a</sup>Department of Physics and Physical Oceanography, Memorial University of Newfoundland, St. John's, NL A1B 3X7, Canada. E-mail: kris@mun.ca; Fax: +1 709 864 8739; Tel: +1 709 864 8890

<sup>b</sup>Max Planck Weizmann Center for Integrative Archaeology and Anthropology, Weizmann Institute of Science, Rehovot, Israel

† Electronic supplementary information (ESI) available: Raw XRD data, comparisons of microstrain fluctuations with lattice strain, raw FTIR data, and grinding curve comparisons for all samples. See DOI: 10.1039/c5ay01942g

‡ Present address: Institut für Naturwissenschaftliche Archäologie, Eberhard Karls Universität Tübingen, Tübingen 72070, Germany.



also the mode that softens (broadens) the most at high temperatures.<sup>10</sup>

Although quantitative analyses of FTIR data are gaining popularity, XRD is still the benchmark method for assessing structural differences in solids. In powder XRD patterns, peak positions provide information about lattice strain:<sup>21,22</sup>

$$\varepsilon_{hkl} = \left( \frac{d - d_0}{d_0} \right)_{hkl}, \quad (1)$$

wherein  $\varepsilon_{hkl}$  is the average elastic strain for a given  $hkl$  direction based on the calculated ( $d$ ) and initial ( $d_0$ ) plane spacings. XRD peak widths are affected by both crystalline domain size  $r$  as well as microstrain fluctuations  $\sigma$ :<sup>23</sup>

$$r = 2d \frac{\tan \theta_B}{W_L}, \text{ and} \quad (2)$$

$$\sigma = \frac{\sqrt{W_G^2 - W_L^2}}{4\sqrt{2} \ln(2) \tan \theta_B}. \quad (3)$$

Here,  $\theta$  is the Bragg diffraction angle, and  $W_L$  is the instrumental broadening. XRD peaks can be fitted with a Voigt function to give the relative amount of Lorentzian contribution  $W_L$  and Gaussian contribution  $W_G$ . This strategy has been used successfully on high-resolution synchrotron XRD data from powders of biogenic and geogenic calcite.<sup>24,25</sup>

It is also possible to extract microstrain fluctuation information from lower resolution XRD data by assessing peak position shifts through the Williamson–Hall relation:<sup>26–29</sup>

$$\text{FWHM} \cos \theta = \frac{K\lambda}{r} + 4\sigma \sin \theta \quad (4)$$

Here,  $r$  is the crystalline domain size,  $\sigma$  is the microstrain fluctuation,  $\lambda$  is the incident X-ray wavelength, and  $K$  is a dimensionless shape factor with a typical value of 0.9 for particles that are rough approximations to spherical. This expression shows a convenient correlation between the full width at half maximum (FWHM) of a given Bragg peak and the diffraction angle at which it occurs ( $2\theta$ ). This analysis is a standard option in XRD software such as Jade (Materials Data Inc.), yet it is not often used in the literature.

In this paper, we demonstrate a clear link between lattice strain, microstrain fluctuations, and crystalline domain size (as obtained from Williamson–Hall analyses of powder XRD data) and relative FTIR peak intensities. We focus on two classes of calcite that are each relevant for archaeological excavations: lime plaster, and calcitic speleothem flowstones. Our data uncover structural differences that are typical for each class. These case studies provide guidance for future investigations based on FTIR screening of calcite-containing samples.

## 2 Experimental details

Calcite lime plasters were made from purchased calcite (Merck) or naturally occurring chalk (Dead Sea, Israel) by heating to 800 °C for 12 hours and then cooling to room temperature. The

product was then mixed with water and aged for various amounts of time (1–7 years) to produce plaster.<sup>1,4</sup> One ancient lime plaster (~10 000 years before present from Yiftahel, Israel) was also studied.<sup>30</sup> Additional comparisons were made by heating a 7 year plaster to 400 °C, which is well below calcite's decomposition temperature. Calcite flowstones were obtained from Manot Cave (Manot, Israel) during archaeological excavations in 2012 and 2013.<sup>31</sup>

The XRD data were collected using either a Rigaku Ultima III or Ultima IV system (each with Cu K $\alpha$  radiation). All XRD data analyses were completed with the Jade software package (Materials Data Inc.),<sup>32</sup> including lattice constant refinements as well as microstrain fluctuation assessments and crystalline domain size values (eqn (4)). For reliable analyses, only well-separated XRD peaks with  $2\theta \leq 70^\circ$  were used. No peak deconvolutions were necessary.

FTIR spectra were obtained using either a Bruker Vertex 70v vacuum spectrometer or a Nicolet 380 N<sub>2</sub>-purged spectrometer. The former was used for measuring commercial calcite and fresh plaster samples (in Canada), while the latter was used to measure all samples (in Israel). All measurements were made in transmission mode over a wavenumber range of 4000 cm<sup>−1</sup> to 500 cm<sup>−1</sup> with a resolution of 1 cm<sup>−1</sup>. Samples were ground with spectral grade KBr and then pressed (2 tons) into transparent 7 mm diameter pellets. IR peak positions and intensities were determined with Bruker's OPUS 7.0 software.

In general, the relative intensities of IR absorbance peaks are affected by the amount and distribution of sample particles in the KBr matrix. To compensate for these variations, and to decouple these effects from changes due to structural differences, we measured many FTIR spectra for each pellet after successive regrinding. Then, we normalized the calcite out-of-plane bend ( $\nu_2$ ) and in-plane bend ( $\nu_4$ ) peak intensities to the intensity of the asymmetric stretch ( $\nu_3$ ) within each spectrum. Results for each spectrum can then be compared to produce a “grinding curve.”<sup>34</sup> These grinding curves decouple the sample preparation influences from factors related to differences in the intrinsic structural order in the material. This procedure and its theoretical foundations are described in detail elsewhere.<sup>8</sup>

## 3 Results

### 3.1 X-ray diffraction analyses

XRD data show that samples used in this study have calcite as the only crystalline phase. The one exception is the freshest plaster (1 year-aged), which contains some Ca(OH)<sub>2</sub> and aragonite. We compare the indexed raw XRD patterns in ESI.† Fig. 1a shows the lattice constant values refined from these XRD data, compared with JCPDS standards.<sup>32</sup> Most flowstones have smaller lattice constants. This is consistent with low levels of Mg incorporation (<6%). Table 1 gives a summary of all lattice constants and the corresponding lattice strains ( $\varepsilon$ , from eqn (1)).

All samples were assessed for angle-dependent XRD peak widths using the Williamson–Hall relation (eqn (4)). Two representative examples are shown graphically in Fig. 2. The first important feature in this plot is the slope of the fits, which is directly proportional to microstrain fluctuation values. For



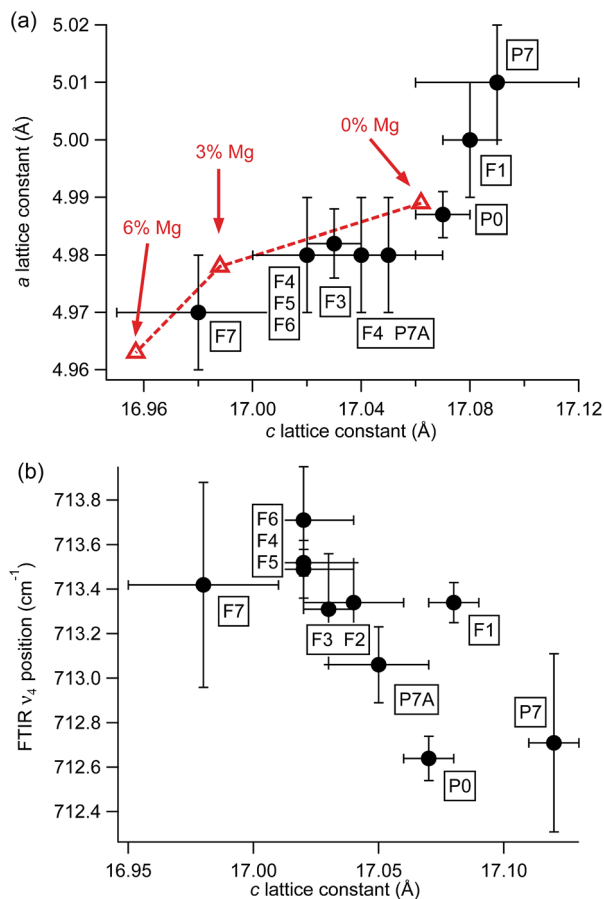


**Fig. 1** (a) Correlations between *a* and *c* lattice constants from XRD data (circles), compared with JCPDS standard patterns for zero- and low-Mg content calcites (triangles). Pure calcite ( $\text{CaCO}_3$ ) is JCPDS 05-0586,  $\text{Mg}_{0.03}\text{Ca}_{0.97}\text{CO}_3$  is JCPDS 97-008-6161, and  $\text{Mg}_{0.06}\text{Ca}_{0.94}\text{CO}_3$  is JCPDS 89-1305. (b) Correlation between *c* lattice constants (from XRD data) and FTIR  $\nu_4$  peak position. Sample labels are defined in Table 1.

data in Fig. 2, this means that the microstrain fluctuation value in sample F4 (a flowstone) is much larger than for sample P0 (a purchased fine-grain calcite). The second important feature

of a Williamson–Hall plot is the *y*-intercept of the fit line, which is inversely proportional to crystalline domain size. Larger domain sizes cause narrower XRD peaks. For the data in Fig. 2, both samples have *y*-intercepts close to zero, which indicates large crystalline domain sizes. In such cases, the peak widths are dominated by other factors, such as instrumental broadening from the diffractometer. Table 1 lists calculated crystalline domain sizes (*r*) and microstrain fluctuation values (*σ*) for all samples. We note that the range of these microstrain fluctuation values are comparable to those reported earlier for calcite from geogenic and biogenic sources.<sup>24</sup>

### 3.2 Fourier transform infrared spectra

FTIR spectra indicate sample compositions that are consistent with XRD data. Peaks due to carbonate vibrational modes are present in all FTIR spectra:  $\nu_3$  (asymmetric stretching near 1430  $\text{cm}^{-1}$ ),  $\nu_2$  (out-of-plane bending near 875  $\text{cm}^{-1}$ ), and  $\nu_4$  (in-plane bending near 713  $\text{cm}^{-1}$ ). Two additional peaks are related to combined modes:<sup>11,14,19</sup>  $\nu_1 + \nu_4$  at 1799  $\text{cm}^{-1}$ , and  $\nu_1 + \nu_3$  at 2512  $\text{cm}^{-1}$ . Only the freshest plaster (P1) shows some  $\text{Ca(OH)}_2$  (3643  $\text{cm}^{-1}$ ) and aragonite (858  $\text{cm}^{-1}$ ). No evidence of other phases, such as amorphous calcium carbonate, was detected in any sample. We note that the presence of aragonite can interfere with assessments of relative peak intensities, since it has a weak peak at the same wavenumber as calcite's  $\nu_4$  and  $\nu_3$  peaks. In this study, we ensured that there was quantitative agreement in the relative FTIR peak intensities for the freshest plaster (P1) and previously reported values for phase-pure calcite plasters.<sup>4,8</sup> A more detailed comparison of the raw FTIR data is included in ESI.†

Like the XRD data, FTIR spectra also provide evidence of Mg incorporation. The  $\nu_4$  peak positions in some samples show slight blue shifts ( $\leq 2 \text{ cm}^{-1}$ ), as displayed in Fig. 1b. These shifts correlate well with lattice constant contractions (Table 1), both of which are consistent with low levels of Mg incorporation.<sup>33,34</sup>

Relative FTIR peak height comparisons among selected samples are shown in Fig. 3. Each set of data points corresponds to a range of different measurement preparations conditions

**Table 1** Crystalline domain size, microstrain fluctuations, and lattice constants calculated from XRD data. Domain size and microstrain fluctuations are calculated according to eqn (4). For narrow XRD peaks, domain sizes cannot be quantified accurately, so they are listed as “large.” Lattice strains are listed for {100} and {001} planes based on eqn (1), using the lattice constants from JCPDS 88-1807 (calcite) as  $d_0$ . Sample P1 has larger uncertainty values because it contains  $\text{Ca(OH)}_2$ , and its peaks overlap with some calcite peaks.

Name	Description	<i>r</i> (nm)	<i>σ</i> (%)	<i>a</i> (Å)	<i>c</i> (Å)	$\epsilon_a$ (%)	$\epsilon_c$ (%)
P0	Purchased powder	Large	$0.006 \pm 0.006$	$4.987 \pm 0.004$	$17.07 \pm 0.01$	0.0(2)	0.0(5)
P1	Plaster, 1 year	$90 \pm 40$	$0.03 \pm 0.04$	$5.0 \pm 0.1$	$17.0 \pm 0.3$	0.2(4)	0.3(5)
P7	Plaster, 7 years	$350 \pm 80$	$0.135 \pm 0.008$	$5.00 \pm 0.01$	$17.09 \pm 0.03$	0.2(4)	0.1(6)
P7A	Plaster, 7 years annealed	$240 \pm 40$	$0.113 \pm 0.008$	$4.98 \pm 0.01$	$17.05 \pm 0.02$	−0.1(6)	−0.0(6)
P10K	Plaster, 10 000 years	$250 \pm 30$	$0.006 \pm 0.006$	$4.983 \pm 0.005$	$17.05 \pm 0.01$	−0.1(0)	−0.0(6)
F1	Flowstone	Large	$0.039 \pm 0.003$	$5.00 \pm 0.01$	$17.08 \pm 0.01$	0.2(4)	0.1(1)
F2	Flowstone	Large	$0.059 \pm 0.005$	$4.98 \pm 0.01$	$17.04 \pm 0.02$	−0.1(6)	−0.1(2)
F3	Flowstone	Large	$0.141 \pm 0.007$	$4.982 \pm 0.006$	$17.03 \pm 0.01$	−0.1(2)	−0.1(8)
F4	Flowstone	Large	$0.161 \pm 0.006$	$4.98 \pm 0.01$	$17.02 \pm 0.02$	−0.1(6)	−0.2(4)
F5	Flowstone	Large	$0.146 \pm 0.008$	$4.98 \pm 0.01$	$17.02 \pm 0.02$	−0.1(6)	−0.2(4)
F6	Flowstone	Large	$0.164 \pm 0.007$	$4.98 \pm 0.01$	$17.02 \pm 0.02$	−0.1(6)	−0.2(4)
F7	Flowstone	Large	$0.195 \pm 0.006$	$4.97 \pm 0.01$	$16.98 \pm 0.03$	−0.4(7)	−0.4(7)



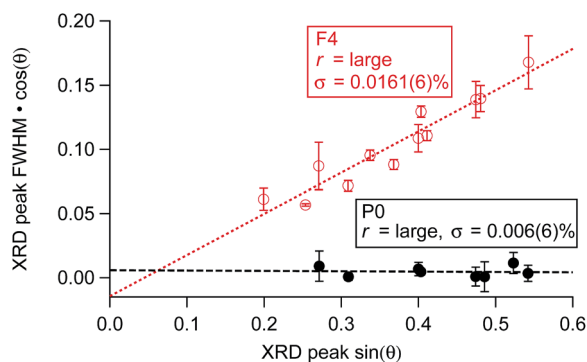


Fig. 2 Representative plots showing angle-dependent XRD peak widths, according to the Williamson–Hall relation. The slopes of the fit lines are directly proportional to microstrain fluctuation values, and the y-intercepts are inversely proportional to crystalline domain sizes.

(grindings) for a single type of sample (as described in Section 2 above). In general, higher normalized  $v_4$  values indicate better crystallinity.<sup>7</sup> Fig. 3a shows that small crystalline domain sizes ( $90 \pm 40$  nm) correlate with a grinding curve shift to lower normalized  $v_4$  values, when lattice strain and microstrain fluctuations are both zero. We note that these grinding curve shifts are quantitatively similar to earlier reports that compared large-grain spar calcite and pure calcite lime plasters (though no crystalline domain sizes were reported).<sup>4,8</sup>

To emphasize that grinding curve shifts cannot be due solely to crystalline domain size differences, Fig. 3b shows that large microstrain fluctuation values ( $0.113(8)\%$ ) also correlate with a grinding curve shift to lower normalized  $v_4$  values (when lattice strain is zero and crystalline domain sizes are large). Fig. 3b shows that annealing a sample to reduce microstrain fluctuations drives the grinding curve to higher  $v_4/v_3$  values for a given  $v_2/v_3$  range, even when the overall crystalline domain sizes remain comparable. In the case shown in Fig. 3b, the crystalline domain sizes for a 7 year plaster shrink only slightly upon annealing (from  $350 \pm 80$  nm to  $240 \pm 40$  nm after 6 hours at  $400^\circ\text{C}$ ), but the microstrain fluctuations drop from  $0.135(8)\%$  to  $0.113(8)\%$  after annealing.

Thus, two different kinds of structural disorder (small crystalline domain sizes, and large microstrain fluctuations) are correlated with the same kind of grinding curve shifts. Finally, Fig. 3c shows that two samples with different kinds of structural disorder can have identical grinding curve shifts. A comparison of FTIR grinding curves for all samples is included in ESI.†

## 4 Discussion

Based on data in Table 1 and in Fig. 3, it is evident that three different kinds of structural disorder ( $\sigma$ ,  $\epsilon$ , and  $r$ ) can affect the relative peak intensities in calcite FTIR spectra. Furthermore, our results show that decoupling these three different kinds of structural disorder is not possible from FTIR grinding curves alone.

It is a new finding that microstrain fluctuations affect grinding curve shifts in a way that is similar to the effect of small crystalline domain sizes. Prior studies compared FTIR

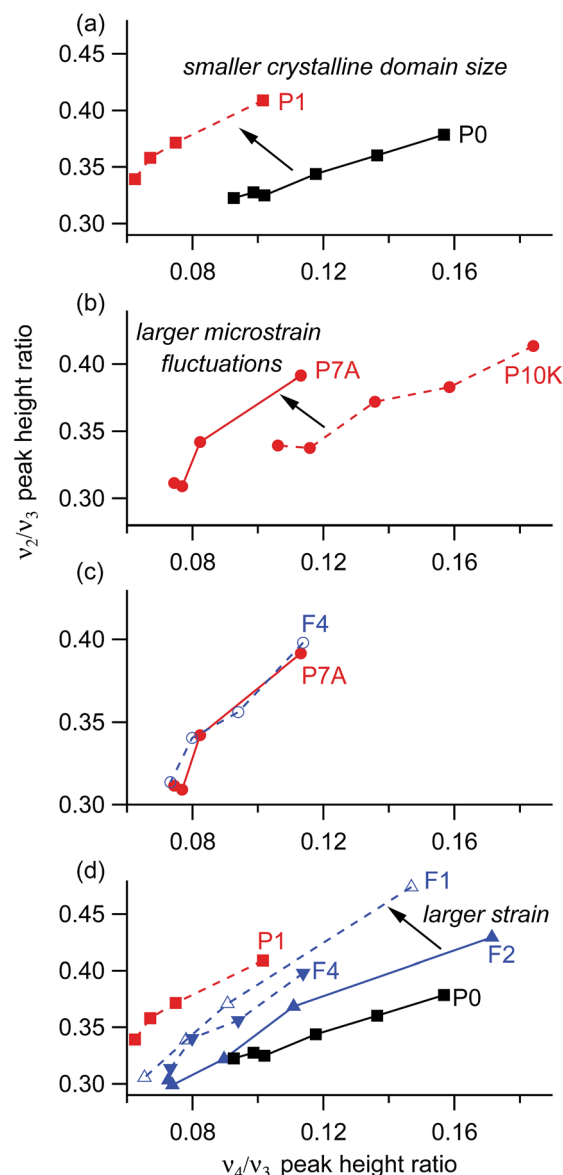


Fig. 3 Representative FTIR grinding curves highlight differences among calcite samples with two distinct kinds of structural disorder. (a) Compares large and small crystalline domain sizes, while (b) compares low and high microstrain fluctuation values. (c) Shows that two samples with different kinds of structural disorder can have identical grinding curve shifts. Comparison in (d) emphasizes that grinding curve shifts cannot be uniquely correlated to a single kind of structural disorder. For clarity, plasters are shown in red, flowstones in blue, and purchased (synthetic) calcite in black.

spectra, XRD data, and DFT for different sources of crystalline calcite, but no explicit suggestions for the underlying structural differences were proposed.<sup>8</sup> More recent studies of aragonite suggested that microstrain fluctuations could influence FTIR peak widths, but no verification was attempted.<sup>35</sup>

Our work also shows that lattice strain, either compression or expansion, can affect grinding curve shifts. This result has support from other studies in the literature, but had not been demonstrated explicitly. An earlier report used high-resolution neutron diffraction data to assess structural differences in





biogenic calcites, including comparisons with FTIR  $\nu_4$  peak positions and widths.<sup>34</sup> Their work used energy-dispersive and wavelength-dispersive X-ray analyses to determine Mg content independently from the lattice constants derived from the diffraction measurements. They used these data to correct for Mg content in their FTIR data, and concluded that all peak position differences can be attributed to Mg levels. In our study, this is consistent with the correlation we see between XRD lattice constants and FTIR  $\nu_4$  peak positions, as presented in Fig. 1.

However, this earlier neutron-diffraction study<sup>34</sup> also found that FTIR peak width differences are not directly correlated with Mg levels. Instead, they found a stronger correlation between FTIR widths and the magnitude of lattice constant changes. They observed lattice contractions in some samples (suggested to be related to Mg incorporation), but reported lattice expansions in other samples (suggested to be related to the presence of an amorphous precursor).

In our study, we also find a correlation between lattice constant changes and FTIR peak attributes. Here, we use grinding curve shifts (normalized FTIR peak height changes) as a proxy for FTIR peak width differences.<sup>8</sup> Since we have evidence that microstrain fluctuations affect grinding curve shifts, isolating the effect of lattice strain requires more careful comparisons. We provide one such example in Fig. 3d among flowstones that all have large crystalline domain sizes. This figure compares the grinding curve for a flowstone with an expanded lattice and low microstrain fluctuations (F1) with two flowstones (F2 and F4) that have zero lattice expansion but higher microstrain fluctuation values. Based on microstrain fluctuation differences alone, one would expect that F1 should have the smallest grinding curve shift. Instead, F1 has a larger shift than F2 or F4, and we attribute this to its larger lattice strain. We provide a comparison of microstrain fluctuation values with lattice strain in the ESI.†

## 5 Conclusions

There is potential for wider societal impact whenever an analysis tool can be used to understand more about the conditions under which a heritage material was likely produced, or altered. This is certainly true for the work we present here, since decoding the formation and diagenesis history of calcite-based materials including geogenic, biogenic, and anthropogenic sources plays a critical role in archaeological interpretations and in heritage restoration efforts. Furthermore, the analyses we describe here could likely be helpful to identify structural differences in other minerals. For example, aragonite<sup>35</sup> and hydroxyapatite<sup>9</sup> have each shown shifts in their grinding curves, but as of yet, no correlations between these grinding curves and Williamson–Hall analyses of XRD data have been reported.

Our results demonstrate that crystalline domain size, microstrain fluctuations, and lattice strain each affect the FTIR spectra of calcite. We emphasize that the methods described here can identify the *effects* of structural disorder, but not the *causes* of structural disorder. This distinction is important. Several common kinds of structural irregularities can change

calcite's FTIR spectrum in similar ways. This underscores the need to pair FTIR spectroscopy with another method (such as XRD) if one wants to determine what kind of structural disorder is present in the calcite. It is true that many different factors during the synthesis and processing of calcite could cause strains, microstrain fluctuations or other structural irregularities. It is also true that these structural irregularities could be correlated with features such as porosity, crystallite size, or morphology. In the present study, we did not undertake an extensive synthesis-based project to try to produce a full range of different structural defects that calcite can accommodate. Instead, we used sample types that would be relevant for the archaeologists and geoscientists who might be the most likely ones to adopt our method. In this context, it is important to comment on how effective FTIR can be as an on-site identification tool for archaeology.

The present work demonstrates that some kinds of archaeological sites, including caves, may be very challenging for using FTIR grinding curve analyses. Most published reports of grinding curve comparisons have focused on open-air sites, or utilized samples made in laboratory settings.<sup>4,8,9,30,35</sup> The flowstones analyzed in the present study were obtained from recent excavations in Manot Cave (Israel). During these excavations, grinding curves were used in an attempt to identify calcitic ash, which is known to have a pronounced grinding curve shift.<sup>4</sup> Flowstone fragments were prevalent in virtually all sediments. As we demonstrate in this work, flowstones can have very different grinding curve shifts, so it is challenging to distinguish ash signatures from the background calcite. Therefore, it was more helpful to use techniques such as optical microscopy and polarized light microscopy to give additional information (on-site) to help distinguish between ash and flowstones.<sup>2</sup> We note that the heterogeneous chemical composition of ash prevents a thorough investigation of the lattice strain and microstrain fluctuation values in this source of calcite.

Even though this work shows that it is helpful to support FTIR measurements with XRD data, the reality is that many archaeological samples are too small in volume, or too precious, to obtain the powder XRD data required for more detailed structural information. For such samples, the best option is to compare with grinding curves for common sources of calcite, including samples with high degrees of structural perfection. This procedure provides a baseline for comparing relative degrees of structural differences, even if the exact type of disorder cannot be identified from the FTIR data alone. In this way, the grinding curves can be an effective means of rapid on-site screening for samples of possible interest, even if the detailed assessments would benefit from more extensive off-site analyses.

## Acknowledgements

We used XRD facilities at Memorial University (Dr Wanda Aylward, CREAT) and at the Weizmann Institute (Dr Isai Feldman). We thank Dr Miryam Bar-Matthews and Dr Avner Ayalon (Geological Survey of Israel) for access to flowstone samples F3, F5, F6, and F7. We also thank Dr Omry Barzilai (Israel



Antiquities Authority) with Prof. Israel Hershkovitz (Tel Aviv University) and Dr Ofer Marder (Ben Gurion University) who led the excavations at Manot Cave. We thank Dr Ianir Milevski and Dr Hamoudi Khalaily (Israel Antiquities Authority) who led the excavations at Yiftahel.

## References

- 1 M. B. Toffolo and E. Boaretto, *J. Archaeol. Sci.*, 2014, **49**, 237–248.
- 2 S. Weiner, *Microarchaeology: beyond the visible archaeological record*, Cambridge University Press, 2010.
- 3 E. Boaretto and K. M. Poduska, *JOM*, 2013, **65**, 481–488.
- 4 L. Regev, K. M. Poduska, L. Addadi, S. Weiner and E. Boaretto, *J. Archaeol. Sci.*, 2010, **37**, 3022–3029.
- 5 F. B. Reig, J. G. Adelantado and M. M. Moreno, *Talanta*, 2002, **58**, 811–821.
- 6 C. N. Trueman, K. Privat and J. Field, *Palaeogeogr., Palaeoclimatol., Palaeoecol.*, 2008, **266**, 160–167.
- 7 R. Gueta, A. Natan, L. Addadi, S. Weiner, K. Refson and L. Kronik, *Angew. Chem., Int. Ed.*, 2007, **46**, 291–294.
- 8 K. M. Poduska, L. Regev, E. Boaretto, L. Addadi, S. Weiner, L. Kronik and S. Curtarolo, *Adv. Mater.*, 2011, **23**, 550–554.
- 9 Y. Asscher, S. Weiner and E. Boaretto, *Adv. Funct. Mater.*, 2011, **21**, 3308–3313.
- 10 B. Xu and K. M. Poduska, *Phys. Chem. Chem. Phys.*, 2014, **16**, 17634–17639.
- 11 C. E. Weir and E. R. Lippincott, *J. Res. Natl. Bur. Stand., Sect. A*, 1961, **65A**, 173–183.
- 12 F. A. Andersen and L. Brecevic, *Acta Chem. Scand.*, 1991, **45**, 1018–1024.
- 13 H. A. Al-Hosney and V. H. Grassian, *Phys. Chem. Chem. Phys.*, 2005, **7**, 1266–1276.
- 14 L. Gago-Duport, M. Briones, J. Rodriguez and B. Covelo, *J. Struct. Biol.*, 2008, **162**, 422–435.
- 15 D. Buti, F. Rosi, B. Brunetti and C. Miliani, *Anal. Bioanal. Chem.*, 2013, **405**, 2699–2711.
- 16 G. Tarquini, S. N. Cesaro and L. Campanella, *Talanta*, 2014, **118**, 195–200.
- 17 V. Chu, L. Regev, S. Weiner and E. Boaretto, *J. Archaeol. Sci.*, 2008, **35**, 905–911.
- 18 M. Prencipe, F. Pascale, C. M. Zicovich-Wilson, V. R. Saunders, R. Orlando and R. Dovesi, *Phys. Chem. Miner.*, 2004, **31**, 559–564.
- 19 L. Valenzano, Y. Noel, R. Orlando, C. Zicovich-Wilson, M. Ferrero and R. Dovesi, *Theor. Chem. Acc.*, 2007, **117**, 991–1000.
- 20 Y. Politi, Y. Levi-Kalishman, S. Raz, F. Wilt, L. Addadi, S. Weiner and I. Sagi, *Adv. Funct. Mater.*, 2006, **16**, 1289–1298.
- 21 S. Qiu, V. B. Krishnan, S. A. Padula, R. D. Noebe, D. W. Brown, B. Clausen and R. Vaidyanathan, *Appl. Phys. Lett.*, 2009, **95**, 141906.
- 22 A. Stebner, D. Brown and L. Brinson, *Acta Mater.*, 2013, **61**, 1944–1956.
- 23 E. Zolotoyabko and J. P. Quintana, *J. Appl. Crystallogr.*, 2002, **35**, 594–599.
- 24 B. Pokroy, A. Fitch and E. Zolotoyabko, *Acta Mater.*, 2006, **18**, 2363–2368.
- 25 H. Leemreize, J. R. Eltzholtz and H. Birkedal, *Eur. J. Mineral.*, 2014, **26**, 517–522.
- 26 G. Williamson and W. Hall, *Acta Metall.*, 1953, **1**, 22–31.
- 27 C. Suryanarayana and M. G. Norton, *X-ray diffraction: a practical approach*, Springer, 1998.
- 28 A. K. Zak, W. A. Majid, M. Abrishami and R. Yousefi, *Solid State Sci.*, 2011, **13**, 251–256.
- 29 V. Mote, Y. Purushotham and B. Dole, *J. Theor. Appl. Phys.*, 2012, **6**, 6.
- 30 K. M. Poduska, L. Regev, F. Berna, E. Mintz, I. Milevski, H. Khalaily, S. Weiner and E. Boaretto, *Radiocarbon*, 2012, **54**, 887–896.
- 31 I. Hershkovitz, O. Marder, A. Ayalon, M. Bar-Matthews, G. Yasur, E. Boaretto, V. Caracuta, B. Alex, A. Frumkin, M. Goder-Goldberger, *et al.*, *Nature*, 2015, **520**, 216–219.
- 32 Joint Commission on Powder Diffraction Standards C International Centre for Diffraction Data, <http://www.icdd.com>, 2003.
- 33 W. D. Bischoff, S. K. Sharma and F. T. MacKenzie, *Am. Mineral.*, 1985, **70**, 581–589.
- 34 E. Zolotoyabko, E. N. Caspi, J. S. Fieramosca, R. B. von Dreele, F. Marin, G. Mor, L. Addadi, S. Weiner and Y. Politi, *Cryst. Growth Des.*, 2010, **10**, 1207–1214.
- 35 M. Suzuki, T. Kogure, S. Weiner and L. Addadi, *Cryst. Growth Des.*, 2011, **11**, 4850–4859.

